






## Article

# Linear and Nonlinear Optical Properties of Iridium Nanoparticles Grown via Atomic Layer Deposition

Paul Schmitt <sup>1,2,†</sup> , Pallabi Paul <sup>1,2,†</sup> , Weiwei Li <sup>3,4</sup>, Zilong Wang <sup>3,4</sup>, Christin David <sup>5</sup> , Navid Daryakar <sup>5</sup> , Kevin Hanemann <sup>1</sup>, Nadja Felde <sup>1</sup>, Anne-Sophie Munser <sup>1,2</sup>, Matthias F. Kling <sup>3,4,6,7</sup>, Sven Schröder <sup>1</sup>, Andreas Tünnermann <sup>1,2</sup> and Adriana Szeghalmi <sup>1,2,\*</sup> 

<sup>1</sup> Fraunhofer Institute for Applied Optics and Precision Engineering IOF, Center of Excellence in Photonics, 07745 Jena, Germany

<sup>2</sup> Institute of Applied Physics and Abbe Center of Photonics, Friedrich Schiller University Jena, 07745 Jena, Germany

<sup>3</sup> Physics Department, Ludwig-Maximilians-Universität Munich, 85748 Garching, Germany

<sup>4</sup> Max Planck Institute of Quantum Optics, 85748 Garching, Germany

<sup>5</sup> Institute of Condensed Matter Theory and Optics and Abbe Center of Photonics, Friedrich Schiller University Jena, 07743 Jena, Germany

<sup>6</sup> Stanford Linear Accelerator Center, Stanford University, Menlo Park, CA 94025, USA

<sup>7</sup> Department of Applied Physics, Stanford University, Stanford, CA 94305, USA

\* Correspondence: [adriana.szeghalmi@iof.fraunhofer.de](mailto:adriana.szeghalmi@iof.fraunhofer.de)

† These authors contributed equally to this work.

**Abstract:** Nonlinear optical phenomena enable novel photonic and optoelectronic applications. Especially, metallic nanoparticles and thin films with nonlinear optical properties offer the potential for micro-optical system integration. For this purpose, new nonlinear materials need to be continuously identified, investigated, and utilized for nonlinear optical applications. While noble-metal nanoparticles, nanostructures, and thin films of silver and gold have been widely studied, iridium (Ir) nanoparticles and ultrathin films have not been investigated for nonlinear optical applications yet. Here, we present a combined theoretical and experimental study on the linear and nonlinear optical properties of iridium nanoparticles deposited via atomic layer deposition (ALD). Linear optical constants, such as the effective refractive index and extinction coefficient, were evaluated at different growth stages of nanoparticle formation. Both linear and nonlinear optical properties of these Ir ALD coatings were calculated theoretically using the Maxwell Garnett theory. The third-order susceptibility of iridium nanoparticle samples was experimentally investigated using the z-scan technique. According to the experiment, for an Ir ALD coating with 45 cycles resulting in iridium nanoparticles, the experimentally determined nonlinear third-order susceptibility is about  $\chi_{\text{Ir}}^{(3)} = (2.4 - i2.1) \times 10^{-17} \text{ m}^2/\text{V}^2$  at the fundamental wavelength of 700 nm. The theory fitted to the experimental results predicts a  $5 \times 10^6$ -fold increase around 230 nm. This strong increase is due to the proximity to the Mie resonance of iridium nanoparticles.

**Keywords:** linear optical properties; nonlinear optical material; iridium nanoparticles; atomic layer deposition; z-scan technique



**Citation:** Schmitt, P.; Paul, P.; Li, W.; Wang, Z.; David, C.; Daryakar, N.; Hanemann, K.; Felde, N.; Munser, A.-S.; Kling, M.F.; et al. Linear and Nonlinear Optical Properties of Iridium Nanoparticles Grown via Atomic Layer Deposition. *Coatings* **2023**, *13*, 787. <https://doi.org/10.3390/coatings13040787>

Academic Editor: Piotr Potera

Received: 13 March 2023

Revised: 10 April 2023

Accepted: 12 April 2023

Published: 18 April 2023



**Copyright:** © 2023 by the authors. Licensee MDPI, Basel, Switzerland. This article is an open access article distributed under the terms and conditions of the Creative Commons Attribution (CC BY) license (<https://creativecommons.org/licenses/by/4.0/>).

## 1. Introduction

Materials with strong nonlinear optical properties enable novel photonic and optoelectronic applications for optical communication and data processing [1,2], optical data storage [3], imaging [4,5], optical limiters [6], ultrafast switches [7], photocatalysis [8], etc. While bulk crystals [9], such as barium borate ( $\beta\text{-BaB}_2\text{O}_4$ ) and lithium niobate ( $\text{LiNbO}_3$ ), have been widely exploited for different nonlinear processes, nanomaterials enable the development of complex nanostructured systems for micro-optical system integration. For instance, metallic nanoparticles (NP) or nanostructures [10] and two-dimensional

(2D) materials [11] exhibit significant nonlinear optical properties due to plasmonic enhancements and quantum-size effects. Among these, localized nanoscopic light sources in fluorescence spectroscopy from Au-nanoring structures incorporated with LiNbO<sub>3</sub> [12]; improved third-order nonlinearities of Au NP in a sapphire matrix [13]; quantum-size effect-based enhancement of third-order nonlinearities in Ag NPs embedded in silica glass [14]; or promising surface-second-harmonic generation from Au, Ag, Al, and W metal stacks [15] are recent developments. Other promising material classes for nonlinear applications include transparent conductive oxide films (e.g., indium tin oxide [16]) and oxide multilayer-based metamaterials (e.g., Al<sub>2</sub>O<sub>3</sub>/ZnO [17] and Al<sub>2</sub>O<sub>3</sub>/TiO<sub>2</sub>/HfO<sub>2</sub> [18]).

While there is significant interest in nonlinear processes in metallic nanomaterials primarily for gold or silver, with their plasmonic resonances residing in the visible, other metals are studied less. For instance, improved optical performance in the ultraviolet (UV) spectral range, further enhancement of nonlinear optical properties, and new nonlinear materials such as various metallic NPs, embedded NPs, and nanostructured metasurfaces need to be identified and investigated. Iridium (Ir) is an exceptionally stable metallic material with high thermal stability and oxidation resistance. In optics, metallic Ir thin films are usually applied as X-ray mirrors [19,20] at grazing incidence due to their high density [21]. Further applications include Fresnel zone plates [22], metal wire grid polarizers in the UV spectral range [23], protection layers [24], and stable and highly reflective Ir mirror coatings for the infrared (IR) spectral range [25]. Iridium complexes with suitable ligands show second-order nonlinear optical and two-photon absorption properties [26]. The linear optical properties of thick metallic Ir films have been reported [25,27,28]; however, ultrathin and partially transparent NP assemblies, mostly relevant for nonlinear optical applications, have not yet been investigated.

This article discusses the linear and nonlinear optical properties of Ir nanoparticles. Samples were prepared via atomic layer deposition (ALD) based on sequential, self-limiting surface reactions, allowing for precise sample-thickness control [29–31]. Iridium nano-sized islands are formed before the growth of a continuous thin film, and by controlling the reaction cycles, NPs of different sizes and surface coverage can be generated [32]. Consequently, the linear and nonlinear optical properties of iridium depend strongly on this stage of growth. Here, a combination of spectroscopic and microscopic tools, including spectrophotometry (SP), spectroscopic ellipsometry (SE), and angle-resolved scattering (ARS), were applied and supplemented with X-ray reflectometry (XRR), white light interferometry (WLI), and scanning electron microscopy (SEM). In previous studies, we extensively investigated the nucleation, layer formation, and morphology of Ir ALD thin films [25,32]. The nonlinear optical properties of Ir ALD coatings were calculated using the Maxwell Garnett theory for their third-order susceptibility [33] and compared with experimentally obtained values using the femtosecond z-scan technique.

## 2. Materials and Methods

**Deposition:** Amorphous fused silica (FS) samples with ultra-flat surfaces were used as substrates. The typical AFM ( $1 \times 1 \mu\text{m}^2$ ) root-mean-square (rms) surface roughness was about 0.26 nm. Their cleaning was performed with a multi-stage, ultrasonic-assisted bath cleaning system (Elma Schmidbauer, Singen, Germany) with alternating surfactants and water (H<sub>2</sub>O) baths followed by a deionized, ultra-pure H<sub>2</sub>O bath.

The depositions were performed with a commercial SunALE R-200 Advanced ALD system (Picosun Oy, Masala, Finland) with iridium(III) acetylacetonate (Ir(acac)<sub>3</sub>) and molecular oxygen (O<sub>2</sub>) as precursors [25,32,34]. A heatable wafer chuck ensured a substrate temperature of 380 °C. One Ir ALD cycle consisted of 6 s of Ir(acac)<sub>3</sub> pulse, 60 s of purge, 2 s of O<sub>2</sub> pulse, and 6 s of purge with molecular nitrogen (N<sub>2</sub>) as the purging gas. By tuning the growth cycles (30–400 cycles), Ir coatings with NPs and ultrathin films were grown with an effective thickness varying between 1.6 nm and 25 nm.

**Characterization:** The structural properties of our Ir coatings were determined through XRR, WLI, and SEM. For the XRR measurements, a D8 Discover diffractometer (Bruker

AXS, Karlsruhe, Germany) with Cu  $K\alpha$  radiation ( $\lambda = 0.154$  nm), 40 kV cathode current, and 40 mA acceleration voltage in Bragg-Brentano geometry was used. A NewView 7300 system (Zygo, Middlefield, CT, USA) with 50 $\times$  magnification was used for WLI measurements. SEM images were obtained with a field-emission SEM Hitachi S-4800 (Hitachi, Tokyo, Japan) using 0.7 kV acceleration voltage and 2.0–3.2 mm working distance. The open-source image processing program ImageJ [35] was used to analyze the SEM images.

The linear optical properties were determined using SP, SE, and ARS. Reflectance  $R$ , transmittance  $T$ , and optical losses  $OL = 1 - R - T$  from 200 nm to 2200 nm were measured with a two-beam spectrophotometer Lambda 900 (PerkinElmer, Waltham, MA, USA) at 6 $^\circ$  angle of incidence. The ellipsometric parameters, including amplitude ratio  $\Psi$  and phase shift  $\Delta$ , from 190 nm to 980 nm were determined with a spectroscopic ellipsometer SE850 DUV (Sentech Instruments, Berlin, Germany) at angles of incidence between 40 $^\circ$  and 70 $^\circ$ . The optical constants of Ir, namely the effective refractive index  $n$  and extinction coefficient  $k$ , were evaluated using the SpetraRay/4 (Sentech Instruments, Berlin, Germany) software package by fitting the  $\Psi$  and  $\Delta$  data. Therefore, a three-layer model consisting of an FS substrate, an effective Ir layer using a Drude–Lorentz model with five oscillators, and the surface roughness as an effective-medium-approximation (EMA) top layer according to Bruggeman were applied. As determined by XRR, the thicknesses of the effective Ir layer and EMA layer were kept constant during the fit procedure. ARS was performed using an ALBATROSS-TT system (Fraunhofer IOF, Jena, Germany) at normal incidence and 405 nm wavelength with a 3 mm illumination spot in forward and backward scattering [36].

Nonlinear optical properties were investigated using the z-scan technique. A home-built non-collinear optical parametric amplifier driven by an Ytterbium-based fiber laser (Active Fiber Systems, Jena, Germany) with a 100 kHz repetition rate was used as the light source. Following this, we selected the fundamental wavelength at 700 nm using a 40 nm bandpass filter resulting from a typical 100 fs pulse. An achromatic lens focused the laser light with a focal length of 10 mm, and the beam waist at the focus position was about 48  $\mu\text{m}$ . The open aperture (OA) and closed aperture (CA) z-scan measurements of the Ir NP layers were performed simultaneously under an average incident power of 80 mW, corresponding to a laser intensity of about 218  $\text{GW}/\text{cm}^2$  at the focus position. Here, the laser intensity was chosen so that the signals from the Ir NP samples could be clearly distinguished from substrate contributions. The samples were mounted on a motorized linear translation stage, which allowed scanning through the beam's focus. In order to reduce the thermal effects accumulated on the sample surfaces, a mechanical shutter was placed in front of the sample. This shutter was switched on for 100 ms for each z-position and then switched off while the sample was moved to the next z-position. The OA and CA signals were detected using two biased Si photodiodes (DET10A2, Thorlabs, Newton, NJ, USA) and then demodulated with two lock-in amplifiers (SR830, Stanford Research Systems, Sunnyvale, CA, USA) at laser repetition rate.

Simulation: The Maxwell Garnett (MG) and Bruggeman (BG) theories [33,37] were employed to model the optical properties of the Ir coatings, using their layer thicknesses and surface coverages as determined using XRR and SEM, respectively. Standard MG assumes spherical material inclusions (Ir) inside a host matrix (air) with a volume fill fraction  $f$  in quasi-static and dipolar approximation. However, particle–particle interactions are not considered, so that MG loses its validity with increasing fill fraction. The local field enhancement factor  $\eta$  for spherical inclusions is

$$\eta = \frac{\varepsilon_1 - \varepsilon_2}{\varepsilon_1 + 2\varepsilon_2} \quad (1)$$

with the permittivity of the spherical Ir inclusions  $\varepsilon_1$  and air as host material  $\varepsilon_2$ . The effective permittivity  $\varepsilon_{\text{MG}}$  in the MG theory is calculated from

$$\varepsilon_{\text{MG}} = \varepsilon_2 \frac{1 + 2f\eta}{1 - 2f\eta} \quad (2)$$

and simulates the permittivity for a homogeneous material consisting of the two materials. This strict quasi-static approximation can be lifted by considering a dipolar Mie term [38], which is relevant for larger particle sizes.

On the other hand, the BG theory enables more complex mixtures of the constituents by not assuming a specific shape but rather by including a polarization factor  $p$ . Moreover, there is no distinction between the composite into a host and inclusion material. The effective permittivity  $\epsilon_{BG}$  is obtained from

$$\sum_{m=1}^2 \frac{\epsilon_m - \epsilon_{BG}}{\epsilon_{BG} + p(\epsilon_m - \epsilon_{BG})} = 0 \quad (3)$$

with an analytical solution for two constituent materials. The corresponding complex refractive index  $\tilde{n} = n + ik$  is obtained from  $\tilde{n} = \sqrt{\epsilon_{EMA}}$ . In thin-film calculations based on Fresnel coefficients, this is used to include the layer thickness of different Ir ALD coatings.

Nonlinear extensions for both MG [39,40] and BG [41,42] theories exist and were adapted to analyze Kerr nonlinearities at the incident frequency for the ultrathin Ir NP layers on FS in air [33]. First, the Mie resonances of Ir NPs with frequencies  $\omega_0(R)$  depending on the particle size  $d = 2R$  were calculated. Second, we adjusted the third-order electron response to a third-order nonlinear bulk susceptibility in Lorentzian form [40,43]:

$$\chi_1^{(3)}(R) = \frac{a}{D(\omega, R)^2 D(\omega, R) D(-\omega, R)} = \frac{a}{D(\omega, R)^2 |D(\omega, R)|^2} \quad (4)$$

with the denominator  $D(\omega, R) = \omega_0^2 - \omega^2 - i\Gamma\omega$  [40]. The contributions of air as a host material and FS as substrate with  $\chi_2^{(3)} = 1.77 \times 10^{-25} \text{ m}^2/\text{V}^2$  and  $\chi_{FS}^{(3)} = 2.5 \times 10^{-22} \text{ m}^2/\text{V}^2$ , respectively, are small compared to the  $\chi_1^{(3)}(\omega \rightarrow 0)$  limit. This is consistent with experimental observations comparing measurements in vacuum and air. The low-frequency limit, known as Miller's rule [44], allows for estimating the nonlinear coefficient in varying host materials, which leads to  $\chi_1^{(3)}(\omega \rightarrow 0) = 1.98 \times 10^{-19} \text{ m}^2/\text{V}^2$  for a particle size of 5 nm. In the composite material, assuming nonlinear properties from both Ir NPs and the host environment, the nonlinear MG expression becomes [39,40]

$$\chi_{\text{eff}}^{(3)} = fv^2|v|^2\chi_1^{(3)} + (1 - f + xf)q^2|q|^2\chi_2^{(3)} \quad (5)$$

with

$$v = \frac{\epsilon_{MG} + 2\epsilon_2}{\epsilon_1 + 2\epsilon_2}, \quad (6)$$

$$q = \frac{\epsilon_{MG} + 2\epsilon_2}{3\epsilon_2}, \quad (7)$$

and

$$x = \frac{8}{5}\eta^2|\eta|^2 + \frac{6}{5}\eta|\eta|^2 + \frac{2}{5}\eta^3 + \frac{18}{5}(\eta^2 + |\eta|^2) \quad (8)$$

All these factors describe different enhancement processes of the system at different orders. With the third-order susceptibility of bulk and Ir coatings, the nonlinear refractive index  $n_2$  and absorption coefficient  $\beta$  are presented in Table S1 in the Supporting Information according to the formalism established previously [44].

Finally, we computed the overall optical properties from  $\vec{P} = \epsilon_0\epsilon_{\text{tot}}(\omega, R)\vec{E}(\omega)$  with

$$E_{\text{tot}}(\omega, R) = \epsilon_{MG}(\omega) + 3\chi_{\text{eff}}^{(3)}(\omega, R)\left|\vec{E}\right|^2 + \chi_{\text{eff}}^{(3)}(3\omega, R)\vec{E}\vec{E}, \quad (9)$$

including Kerr nonlinearities at the fundamental wavelength (FH). The third harmonic term was considered separately for evaluating third-harmonic generation processes as it gives vanishing contributions far-off its resonance. This material model, together with

the scattering matrix theory, was used to describe a system of effectively homogeneous layers [33].

### 3. Results

**Linear optical properties.** Figure 1 shows the measured reflectance  $R$ , transmittance  $T$ , and calculated optical losses  $OL = 1-R-T$  spectra of Ir ALD coatings on FS substrates with ALD cycles varying from 30 to 400 cycles. With increasing ALD growth cycles, initial changes in the optical properties emerge in the deep ultraviolet (DUV) spectral range for small cycle numbers. While the reflectance of the Ir coatings up to 45 cycles (light green) is nearly identical to the bare FS substrate (red), the transmittance around 200 nm wavelength decreases, and consequently, the optical losses increase. These coatings are in the regime of nanoparticle growth, as confirmed through extensive SEM investigations [32]. Further information on the surface roughness of such Ir coatings by means of atomic force microscopy (AFM) was incorporated in detail in our previous work [32]. With several tens of cycles, the grown Ir NPs have a weak Mie scattering of localized surface plasmons, and more intense interband transitions dominate in the DUV spectral range. About 60 Ir ALD cycles lead to about 20% optical losses around the 230 nm wavelength with very low scattering losses (see also Table 1).

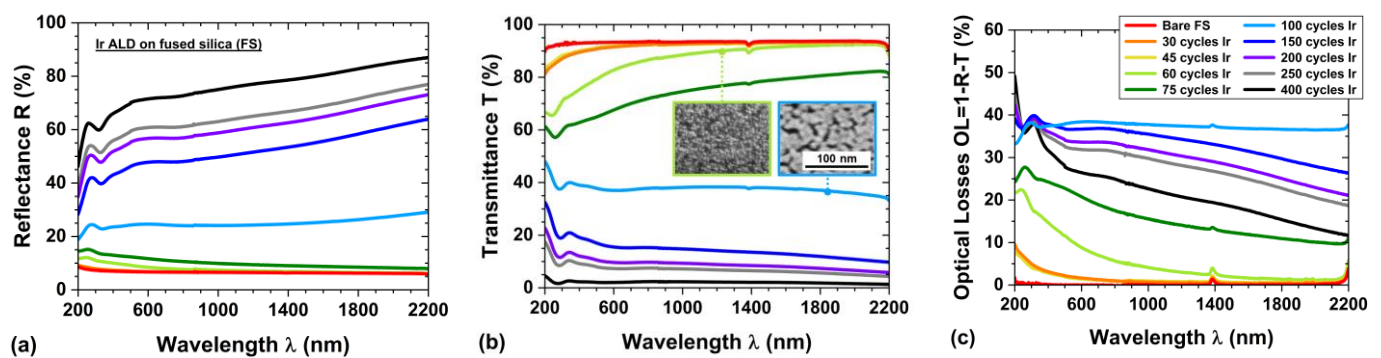


**Figure 1.** (a) Reflectance, (b) transmittance, and (c) optical losses of iridium (Ir) coatings deposited on fused silica (FS) using different atomic layer deposition (ALD) cycles. Additionally, top-view scanning electron microscopy (SEM) images are shown for selected coatings with 60 and 100 ALD cycles in which Ir appears bright on the dark-appearing FS surface.

**Table 1.** Properties of Ir ALD coatings deposited on FS. The effective Ir layer thickness and density were analyzed using X-ray reflectometry (XRR), white light interferometry (WLI), and XRR for surface roughness.

Sample ID	Number of ALD Cycles	Ir Thickness XRR (nm)	Ir Density XRR ( $\text{g}/\text{cm}^3$ )	Ir Surface Roughness (nm)		Optical Losses @ 405 nm (%)	Total Scattering @ 405 nm (ppm)
				XRR	WLI		
1	30	$1.6 \pm 1.0$	$8.5 \pm 2.0$	$0.4 \pm 0.2$	$0.5 \pm 0.1$	$3.1 \pm 0.5$	$174 \pm 17$
2	45	$2.0 \pm 1.0$	$4.1 \pm 2.0$	$0.8 \pm 0.2$	-	$2.7 \pm 0.5$	$40 \pm 4$
3	60	$3.0 \pm 1.0$	$11.8 \pm 1.0$	$1.0 \pm 0.2$	$0.5 \pm 0.1$	$14.5 \pm 0.5$	$252 \pm 25$
4	75	$4.0 \pm 1.0$	$18.0 \pm 1.0$	$1.2 \pm 0.2$	-	$24.2 \pm 0.5$	-
5	100	$5.7 \pm 1.0$	$20.1 \pm 0.5$	$0.9 \pm 0.2$	$0.6 \pm 0.1$	$37.5 \pm 0.5$	$711 \pm 71$
6	150	$8.7 \pm 1.0$	$22.5 \pm 0.5$	$1.4 \pm 0.2$	$0.9 \pm 0.1$	$37.8 \pm 0.5$	$79 \pm 8$
7	200	$11.7 \pm 1.0$	$22.3 \pm 0.2$	$1.2 \pm 0.2$	$0.9 \pm 0.1$	$36.0 \pm 0.3$	$236 \pm 24$
8	250	$14.3 \pm 1.0$	$22.3 \pm 0.2$	$1.1 \pm 0.2$	$0.4 \pm 0.1$	$34.8 \pm 0.3$	$217 \pm 22$
9	400	$24.7 \pm 1.0$	$22.4 \pm 0.1$	$0.9 \pm 0.2$	$0.4 \pm 0.1$	$31.5 \pm 0.3$	$87 \pm 9$

From about 100 Ir ALD cycles, the reflectance increases significantly in the whole spectral range from 200–2200 nm. As an indicator for the formation of continuous metallic



films, such an increase in reflectance was also reported in evaporated Au [45] and Ag [46] coatings. Iridium coatings with more than 75 cycles exhibit pronounced OL of about 10%–40% in the IR spectral range. The initial Ir ALD thin-film formation follows the Volmer–Weber growth type. Similar to physical vapor deposition processes, these small Ir NPs continuously grow, coalesce, form a coherent network, and finally form a closed ultrathin film (see also Supplementary Figure S1). The sizes of the isolated NPs range from 2–20 nm [32], which results in absorption and low Mie scattering in the UV spectral range. The total scattering (TS) of these Ir coatings, depending on their number of ALD cycles, is given in Table 1 and Supplementary Figure S4. This total scattering is most pronounced at 100 ALD cycles when an interconnected network has formed. However, the total scattering with  $TS < 0.1\%$  is negligible compared to the overall optical losses of up to 40%, which means that (dissipative) absorption mainly causes the optical losses. Therefore, the exceptionally high absorption at 100 cycles could be mainly due to the light confinement effect, particularly in the IR region. For comparison, the OL and TS of these Ir ALD coatings, as well as their effective layer thicknesses, densities, and surface roughnesses, are listed in Table 1.

The effective linear refractive index  $n$  and extinction coefficient  $k$  of the Ir coatings were determined using spectroscopic ellipsometry. The accuracy of this ellipsometry analysis is supported by variable angle spectroscopic ellipsometric measurements, as summarized in Supplementary Figures S2 and S3. A good agreement between the measured and fitted  $\Psi$  and  $\Delta$  parameters can be seen for angles of incidence between  $40^\circ$  and  $70^\circ$ . Figure 2a,c demonstrate the dispersion profiles of Ir coatings up to 400 ALD cycles. For thin and fully closed Ir films, the determined optical constants reach nearly the bulk values. While the system remains in the NP growth regime up to 45 ALD cycles, the optical constants are relatively low. As the Ir NP system approaches the percolation threshold between 75 and 100 cycles, a significant rise in the optical constants can be observed.

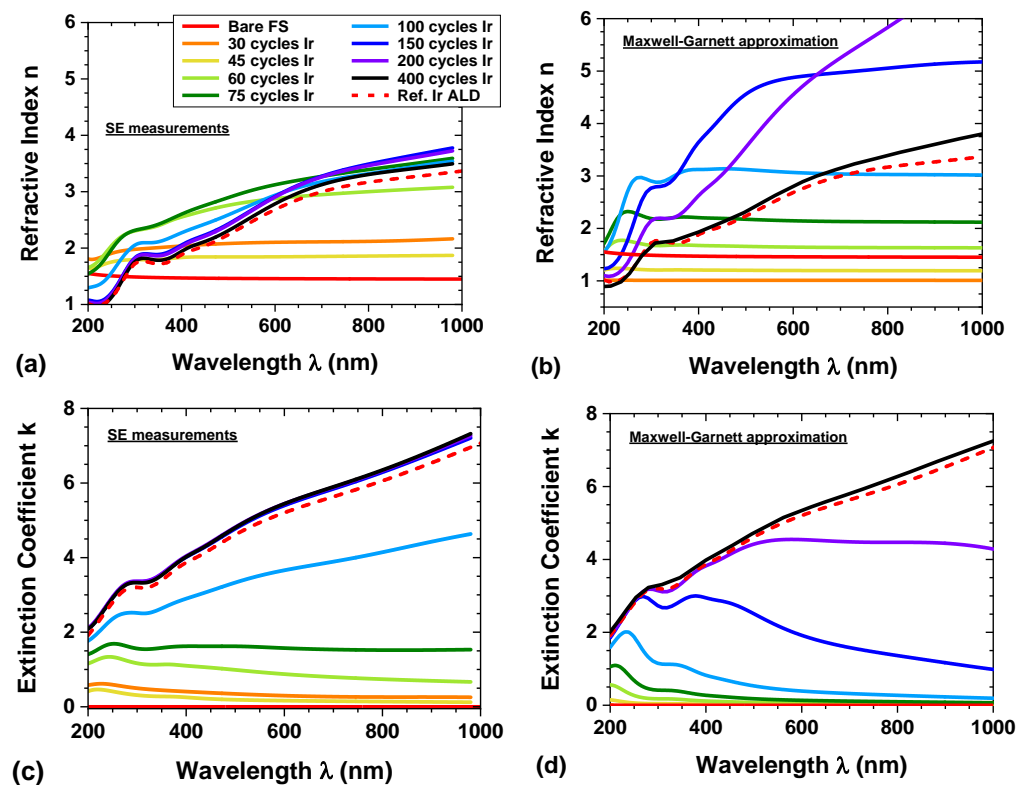


**Figure 2.** Optical constants of Ir coatings with different numbers of ALD cycles from the 200 to 1000 nm wavelength. The refractive index and extinction coefficient were evaluated by fitting (a,c) spectral ellipsometry (SE) measurements and modeled using (b,d) the Maxwell Garnett (MG) theory.

Additionally, the effective optical constants were numerically simulated using the Maxwell Garnett (MG) approach, wherein spherical Ir NPs are embedded in a host (air) matrix. Figure 2b provides a rough estimation of these dispersion profiles showing an increasing trend in the refractive index  $n$  as the Ir surface coverage increases. However, the extinction profiles were not suitably predicted by the MG model, especially for Ir coatings above the percolation threshold, as the MG approach is limited to a higher fill fraction of iridium inclusion. In addition, the large extinction coefficient of metallic inclusions and the resulting strong contrast in the refractive index to the host material lead to discrepancies in EMA theories. The growth of iridium in the nucleation regime depends very much on the process conditions, and slight deviations in the sizes of the particles or the surface coverages result in significant variations in the reflectance, transmittance, and optical losses.

The third-order nonlinearity of Ir NP systems with 30, 45, and 60 ALD cycles was then investigated experimentally using the z-scan technique. Figure 3 shows a typical measurement for an Ir NP coating with 45 cycles. The normalized open aperture (OA) measurement shows a weak positive peak at around  $Z = 0$ , while no OA signal can be found from bare FS. The positive OA signal corresponds to saturable or two-photon absorption. This result can be fitted as follows:

$$T(x) = \sum_{m=0}^{\infty} \frac{[-q_0]^m}{(m+1)^{3/2}}, \tag{10}$$

$$q_0 = \frac{\beta I_0 L_{\text{eff}}}{1+x^2}, \tag{11}$$

where  $x = z/z_0$ ,  $z_0$  is the diffraction length of a Gaussian laser beam,  $\beta$  is the nonlinear absorption coefficient,  $L_{\text{eff}} = (1 - e^{-\frac{\alpha_0}{L}})/\alpha_0$  is the sample's effective length,  $\alpha_0$  is the sample absorption coefficient, and  $L$  is the sample thickness. The values of  $\alpha_0$  can be extracted from the linear measurement results. The fitted  $\beta$  value for the sample with 45 Ir ALD cycles is  $-3.35 \times 10^{-8}$  m/W.

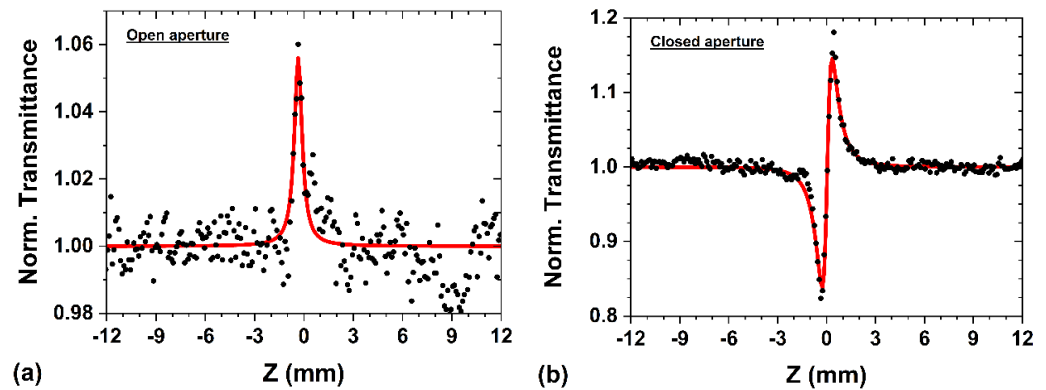


Figure 3. Normalized transmittance of z-scan measurements for (a) open aperture (OA) and (b) closed aperture (CA) for an Ir coating with 45 ALD cycles.

In the CA measurement, the derivative shape curve originates from the nonlinear Kerr effect of the material. As shown in Figure 3b, the normalized CA transmittance first decreases for the sample at the position before the focus ( $Z < 0$ ) and then increases after the focus ( $Z > 0$ ). This curve indicates a positive Kerr effect, corresponding to self-focusing in the sample. Normalized CA transmittance can be fitted with the following formula [47]:

$$T(x) = 1 + \frac{4x\Delta\Phi}{(1+x^2)(9+x^2)} + \frac{4(3x^2-5)\Delta\Phi^2}{(1+x^2)^2(9+x^2)(25+x^2)} + \frac{32(3x^2-11)x\Delta\Phi^3}{(1+x^2)^3(9+x^2)(25+x^2)(49+x^2)}, \tag{12}$$

where  $\Delta\Phi$  is the on-axis phase shift and  $\Delta\Phi = 2\pi/(\lambda n_2 I_0 L_{\text{eff}})$ ,  $\lambda$  is the fundamental wavelength,  $I_0$  is the on-axis intensity at the focus, and  $n_2$  is the fitting parameter for the Kerr coefficient. Since the bare FS substrate contributes significantly to the CA signal, the actual  $n_2$  value of the sample is obtained by subtracting the fitted  $n_2$  value of the substrate measured separately as a reference (see Supplementary Figure S6). The  $n_2$  of the sample can be obtained as  $1.86 \times 10^{-15} \text{ m}^2/\text{W}$ , and the one measured from the bare FS substrate is around  $\sim -2.11 \times 10^{-20} \text{ m}^2/\text{W}$ . The measured  $n_2$  value of the bare FS agrees well with the results reported [48,49], which could verify the fidelity of our measurement. The relatively large  $n_2$  arises from the Ir NP sample. The thermal effect could affect the measured  $n_2$  value; note that our laser pulse duration is about 100 fs and thus the thermal effect arising from the acoustic wave can be neglected [50].

The real part and imaginary part of the third-order susceptibility  $\chi^{(3)}$  of the samples can be calculated in SI units:

$$\chi_{Re}^{(3)} = \left(\frac{4}{3}\right) n_0 \epsilon_0 c (n_0 n_2 - k_0 k_2) \quad (13)$$

and

$$\chi_{Im}^{(3)} = \left(\frac{4}{3}\right) n_0 \epsilon_0 c (n_0 k_2 + k_0 n_2), \quad (14)$$

where  $n_0$  and  $k_0 = \lambda\alpha/4\pi$  are the linear refractive index and extinction coefficient, respectively, and  $k_2 = \lambda\beta/4\pi$  is the nonlinear extinction coefficient. The experimentally determined  $n_2$ ,  $\beta$ , and  $\chi^{(3)}$  values of the three measured samples are given in Table 2.

**Table 2.** Experimental (exp) and simulated (sim; with fitted third-order susceptibility at 700 nm wavelength) values of nonlinear refractive index  $n_2$ , nonlinear absorption coefficient  $\beta$ , and third-order susceptibility  $\chi^{(3)}$  of selected Ir NP samples at the 700 nm fundamental wavelength.

Number of ALD Cycles	$n_2$ ( $10^{-15} \text{ m}^2/\text{W}$ ) (exp)	$n_2$ ( $10^{-15} \text{ m}^2/\text{W}$ ) (sim)	$\beta$ ( $10^{-8} \text{ m/W}$ ) (exp)	$\beta$ ( $10^{-8} \text{ m/W}$ ) (sim)	Ir Susceptibility ( $10^{-17} \text{ m}^2/\text{V}^2$ ) (exp)		Ir Susceptibility ( $10^{-17} \text{ m}^2/\text{V}^2$ ) (sim)	
					Re( $\chi^{(3)}$ )	Im( $\chi^{(3)}$ )	Re( $\chi^{(3)}$ )	Im( $\chi^{(3)}$ )
30	$1.77 \pm 0.11$	4.22	$-4.01 \pm 0.33$	-7.44	$3.24 \pm 0.21$	$-3.17 \pm 0.27$	3.52	-3.41
45	$1.86 \pm 0.10$	2.15	$-3.35 \pm 0.27$	-3.52	$2.44 \pm 0.14$	$-2.08 \pm 0.17$	2.66	-2.24
60	$1.69 \pm 0.13$	2.95	$-2.88 \pm 0.12$	-3.54	$6.53 \pm 0.35$	$-3.53 \pm 0.32$	7.28	-3.80

Simulations of the third-order nonlinearity of Ir NP systems were performed in the framework of nonlinear MG theory at wavelengths following the z-scan measurements. Figure 4a,b compare the experimentally determined third-order effective susceptibility as a function of the fill fraction with the prediction from Miller's rule. Both the bulk nonlinearity in terms of the third-order susceptibility from Equation (4) and effective susceptibility from MG theory Equation (5) do not show substantial variation with particle size. Thus, they are assumed to be constant at the 700 nm FH far-off the resonance and third harmonic (TH, 233.3 nm) (see Figures 4c and S5). The NP size distribution in the films should be accounted for when particle sizes are above 10 nm or when the fundamental is particularly close to the local surface plasmon resonance. Due to the amorphous mixing of Ir NPs with air on the FS substrate, the effective third-order nonlinear susceptibility is strongly reduced in films with low particle density, represented by the volume fill fraction  $f$ . Here, we consider the three films with the lowest effective thickness according to Table 1. Increasing the fill fraction further leads to unphysical results from this EMA, as already seen for the linear results. Fully closed films are correctly represented by the  $f = 1$  (bulk) limit. Larger fill fractions, as shown in Supplementary Figure S5b, yield a stronger nonlinear response (real part of the susceptibility, solid lines); however, the absorption (imaginary part of the susceptibility represented by dashed lines) is also increased and added to the linear permittivity with the third power of the local fields. At some larger NP densities, the absorption starts to dominate. Our comparative study reveals that the theoretical calculations predict a



$15 \times 10^5$ -fold increase in the bulk susceptibility at the fundamental wavelength (700 nm) when amorphous gold films were used instead of iridium. In contrast, an enhancement for the iridium films grown with 60 ALD cycles is predicted around the 233 nm wavelength. Compared to the fundamental wavelength applied in these experiments, the effective susceptibility using the DUV wavelength ( $\approx 233$  nm) is about  $5 \times 10^6$ -fold larger than at 700 nm. These differences between the metals arise in the local field enhancement at the FH. While gold reaches enhancement factors  $\sim 100$ , the enhancement factors of iridium in Equation (5) are in the order of  $\sim 1 \dots 35$  at the 700 nm wavelength. More cases are discussed in the Supplementary Material and in our previous work [33].

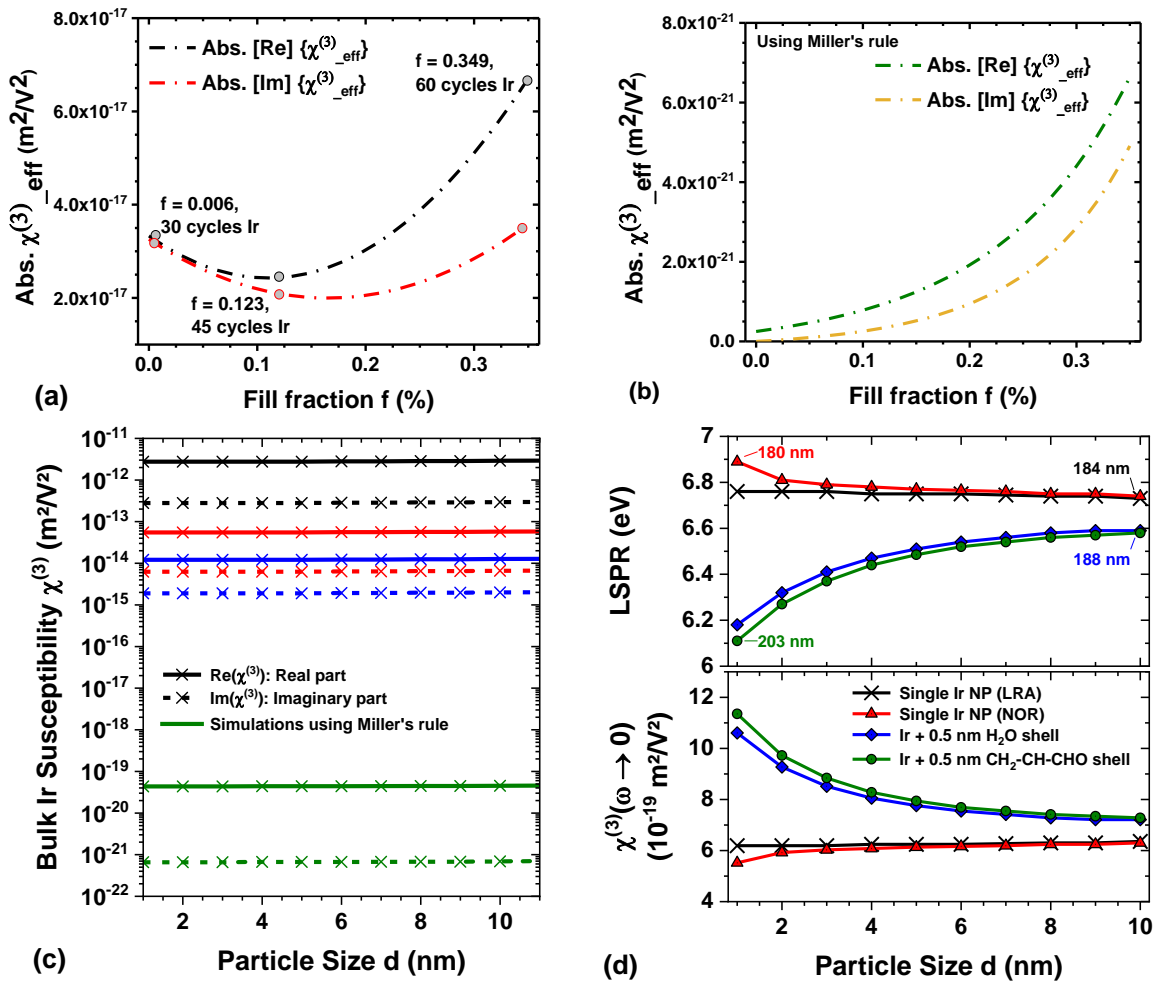


**Figure 4.** (a,b) Real and imaginary parts of the effective susceptibility at the 700 nm fundamental wavelength (FH) for Ir coatings depending on the fill fraction. (a) The values with experimentally determined  $\chi^{(3)}$  and fill fraction values. (b) Values derived from Miller's rule. (c) Bulk Ir susceptibility; the real (solid) and imaginary (dashed) parts are shown for data fitted to the three experimental results, yielding three slightly different nonlinear coefficients  $a = b\omega_p^8$ , with  $b = (-1.12 - i0.15) \times 10^{-15} m^2/V^2$  (blue curves),  $b = (-5.08 - i0.46) \times 10^{-15} m^2/V^2$  (red curves),  $b = (-2.55 - i0.2) \times 10^{-13} m^2/V^2$  (black curves), and the result according to Miller's rule (green curves). (d) Shift of the localized surface plasmon resonance (LSPR, top panel) and Ir susceptibility according to Miller's rule (bottom panel) affected by an ultrathin shell of water (blue) and CH<sub>2</sub>-CH-CHO (green) surrounding the Ir nanoparticles in air. In addition, we compared single Ir NP in the classical local response approximation (LRA, black curves) and the size-induced quantum shift from the nonlocal optical response (NOR, red curves).

We explored the influence of thin coatings around the Ir NPs using impurities such as a water film ( $n = 1.33$ ) or a shell of CH<sub>2</sub>-CH-CHO (acrylic aldehyde,  $n = 1.367$ ) in Figure 4d.

The upper panel shows the dependence of the local surface plasmon resonances of Ir NPs in air with varying sizes. Uncoated Ir NPs (black curves) show a negligible dependence on size, as discussed above, which is the classical Mie result within the local response approximation (LRA). Quantum-size and confinement effects can be included through nonlocal optical response (red curves, NOR) [51]. These effects lead to a blueshift in the resonance position (red curves), effectively reducing third-order susceptibility. However, the effect of a thin 0.5 nm coating on the resonance position is much stronger than the finite-size effect. The refractive indices of pure water and the considered CH<sub>2</sub>-CH-CHO compound are close to each other, therefore, the observed redshift from the Ir-core-shell structures is similar (blue and green curves). Through Equation (4), this resonance shift enters the third-order nonlinear susceptibility shown for the low-frequency limit following Miller's rule in the lower panel of Figure 4d. For the smallest Ir NP size, the presence of an aqueous coating can increase the susceptibility by up to one order of magnitude, pushing the Mie resonance of Ir NPs closer to the wavelength of the incoming laser field.

Thus, the considered coating brings the susceptibilities closer to the experimentally observed values compared to the standard approach and hints towards the importance of considering a thin film of water or hydrocarbon forming on the Ir NPs exposed to air.

Two central problems arise in this theoretical description. Firstly, this approach to nonlinear optical properties of amorphous Ir thin films is instantaneous, and the shape and duration of the excitation pulse are not accounted for. Studies on gold films [52] show that the length of the pulse duration has a tremendous impact on the third-order nonlinear susceptibility, shifting it over orders of magnitude for longer pulses. However, our theoretical result, being instantaneous, is at the limit of vanishing pulse duration. Several orders of magnitude worth of differences between theoretical results and measurements are, thus, not surprising. This could be amended by fitting the power law observed in gold [52] to our Ir coatings by measuring their nonlinear optical response for varying pulse durations and accounting for this effect in calculating the nonlinear susceptibility.

Second, the 233 nm wavelength is very close to the Mie resonance of nano-sized Ir particles. Thus, the effective Ir susceptibility values are largely increased compared to the off-resonant case at the fundamental wavelength of 700 nm, which was used here and can become even larger than the corresponding bulk values. Additionally, the amorphous mixing in the Maxwell Garnett theory at very low fill factors is dominated by the nonlinearity of the host, which defines a lower limit. Air has a nonlinear coefficient several orders of magnitude lower than the FS substrate; however, the influence of a substrate cannot be accounted for within the MG theory. As the studied Ir NP layers are only a few nanometers thick, their interactions with the substrate cannot be neglected (compare Supplementary Figure S5 for Ir NP at the FS/air interface). A self-consistent approach for the nonlinear optical properties of thin amorphous composite films depending on their thicknesses was recently realized in our work [33].

Extensive studies have been conducted on different gold nanoscale systems using the z-scan technique. For example, the nonlinear refractive index  $n_2$  of Au NP in colloid [53] shows  $\approx 1$  to  $2 \times 10^{-17}$  m<sup>2</sup>/W, an Au-SiO<sub>2</sub> composite system [54,55] indicates an  $n_2$  of  $0.4$  to  $8.9 \times 10^{-14}$  m<sup>2</sup>/W, and a periodic nanostructured film [56] of 14 nm gives rise to  $n_2$  of  $9.2 \times 10^{-13}$  m<sup>2</sup>/W. An increase in  $n_2$  has been observed in Au NP aggregate film ( $\approx 9.2 \times 10^{-13}$  m<sup>2</sup>/W) due to local field enhancement compared to 8 nm Au film [57] possessing  $n_2$  of  $6.5 \times 10^{-13}$  m<sup>2</sup>/W. Various studies reported on the nonlinear optical response from a wide range of nanoscale materials, such as large  $n_2$  in an indium tin oxide layer ( $6 \times 10^{-14}$  m<sup>2</sup>/W) at epsilon-near-zero conditions [16], 2D WS<sub>2</sub> [47] with an  $n_2$  of about  $8 \times 10^{-13}$  m<sup>2</sup>/W, two-photon absorption coefficient of TiO<sub>2</sub> thin films [58] at about  $2$ – $5 \times 10^{-13}$  m/W, 5 nm Au thin film [59] with a nonlinear absorption coefficient as large as  $\approx 1.9$  to  $5.3 \times 10^{-5}$  m/W, and 2D BiOBr nanoflakes with  $n_2 \approx 10^{-14}$  m<sup>2</sup>/W and  $\beta \approx 10^{-7}$  m<sup>2</sup>/W, respectively [60]. Hence, compared to other nanoscale materials, the third-order nonlinear optical response of 3–5 nm Ir coatings possesses decent strength. With the incorporation of such ultrathin Ir NPs in various dielectric matrices, one could pave the way to signal enhancement.

Currently, such composite materials are being investigated for both second and third-harmonic generation at VIS/NIR wavelengths.

While the nonlinear refractive index of Ir nanoparticles at the 700 nm wavelength ( $n_2 \sim 10^{-15} \text{ m}^2/\text{W}$ ) is slightly lower than for the materials mentioned above, a promising enhancement is predicted when using a DUV fundamental wavelength at 233 nm. Noteworthy, such large nonlinear optical constants are obtained for the above-mentioned materials at particular wavelengths with strong enhancement conditions. Epsilon-near-zero conditions typically lead to these large nonlinearities, while off-resonance values are lower by 3–4 orders of magnitude. The Mie resonance condition of Ir possibly enhances the nonlinear optical properties at DUV wavelengths. However, the expected TH wavelength is in the vacuum UV range, and such measurements cannot currently be carried out in our laboratories. Further developments in high-power, ultrashort pulsed UV lasers would open new possibilities to investigate such novel material systems. The search for new and stable material systems is essential to address these applications.

#### 4. Conclusions

In this work, we systematically investigated the linear and nonlinear optical properties of Ir nanoparticle coatings grown via atomic layer deposition. Various spectroscopic and microscopic techniques have been applied to probe the linear optical properties of these Ir NP systems. The variation in linear optical properties (e.g., optical spectra, dispersion profiles) is evident based on the nanoparticle density of Ir NP coatings. Further, we implemented a combined experimental and theoretical approach to estimate the third-order susceptibility of Ir NP coatings. A large third-order susceptibility ( $\approx 10^{-17} \text{ m}^2/\text{V}^2$ ) was observed using the z-scan technique with 3–5 nm Ir functionalization. This work demonstrates the potential of ultrathin Ir NPs as an alternative nonlinear optical material at an atomic scale. This approach opens a gateway to develop new engineered materials, for instance, based on incorporating iridium within dielectric matrices, and explore the tunability of their material properties. Increasing interest in deep and vacuum ultraviolet nonlinear applications might prompt the use of such materials.

**Supplementary Materials:** The following supporting information can be downloaded at: <https://www.mdpi.com/article/10.3390/coatings13040787/s1>, Figure S1. (a) Effective Ir layer thickness (black) and layer density (red) of iridium coatings deposited on fused silica (FS) depending on the number of atomic layer deposition (ALD) cycles. In certain regions, the film growth is linearly fitted (black and blue lines) with corresponding growth per cycle (GPC) and nucleation delay (ND) indicated. (b) Surface coverage (black) and layer density (red) determined using scanning electron microscopy (SEM) images and X-ray reflectometry (XRR), respectively, with exponentially saturating fit curves (black and red lines) depending on the Ir layer thickness. Figure S2. Experimental and fitted ellipsometric amplitude ratio (black) and phase shift (red) of Ir coatings with (a) 30, (b) 100, and (c) 250 ALD cycles. The ellipsometric parameters (exemplary at  $70^\circ$  angle of incidence) were fitted using a Drude–Lorentz model with five oscillators, considering the surface roughness with an effective-medium-approximation (EMA) layer. Figure S3. Experimental and fitted data of the ellipsometric (a) amplitude ratio and (b) phase shift of an Ir coating with 75 ALD cycles. The ellipsometric parameters at different angles of incidence were fitted with excellent agreement over the whole spectral range. Figure S4. (a) Angle-resolved scattering (ARS) of selected Ir coatings whereby the scatterometer measures the entire forward and backward hemisphere. (b) Total scattering (TS, black), consisting of near-angle scattering (red) and far-angle scattering (blue), of Ir coatings depending on their number of ALD cycles measured at the 405 nm wavelength. Scattering is most pronounced at 100 cycles but overall negligible compared to the dissipative absorption. According to ISO 13696, total scattering is determined through the ARS integration from  $\theta_s = 2.0\text{--}85^\circ$  in all directions; near-normal ARS from  $2.0\text{--}30^\circ$ ; far-normal ARS from  $30\text{--}85^\circ$ . Figure S5. (a) Bulk Ir susceptibility with the real (solid) and imaginary (dashed) parts shown separately. Next to fitting the three selected samples, we show the case based on Miller’s rule (green curves). (b) Real and (c) imaginary parts of the effective Ir susceptibility for amorphous Ir coatings depending on particle size, using the experimentally determined fill fraction and layer thickness at the 233 nm wavelength.

The solid curves originate from the experimentally fitted z-scan data at different ALD cycles, and the dashed curves are derived from Miller's rule. Table S1. Third-order nonlinear susceptibility calculated from the nonlinear Maxwell Garnett theory with fitting to experimentally obtained values for different samples. Table S2. Third-order nonlinear susceptibility as calculated from nonlinear Maxwell-Garnett theory using Miller's rule to obtain an analytic nonlinear amplitude. Figure S6. Normalized z-scan closed aperture (CA) transmittance of a barefused silica substrate: experimental data (black dots) and the fitted result (solid red curve).

**Author Contributions:** Conceptualization, A.S.; methodology, P.S., P.P., W.L., Z.W., C.D., N.D., K.H., N.F. and A.-S.M.; investigation, resources, P.S., P.P., W.L., Z.W., C.D., N.D., K.H., N.F., A.-S.M., M.F.K. and S.S.; data curation, P.S. and P.P.; writing—original draft preparation, P.S.; writing—review and editing, P.S., P.P., Z.W., C.D., N.D. and A.S.; supervision, M.F.K., S.S., A.T. and A.S.; project administration, A.T. and A.S.; funding acquisition, A.T. and A.S. All authors have read and agreed to the published version of the manuscript.

**Funding:** We acknowledge support from the Fraunhofer Society Attract Project (066-601020), Fraunhofer IOF Center of Excellence in Photonics, and the Deutsche Forschungsgemeinschaft (DFG, German Research Foundation) Collaborative Research Center (CRC/SFB) 1375 "NOA–Nonlinear Optics down to Atomic scales" (398816777). Paul Schmitt thanks the Thüringer Aufbaubank (TAB) for promoting his doctoral research studies. Weiwei Li and Matthias F. Kling acknowledge support from the Max Planck Society via the IMPRS for Advanced Photon Science and the Max Planck Fellow program, respectively. Zilong Wang is grateful for support from the Alexander von Humboldt foundation.

**Institutional Review Board Statement:** Not applicable.

**Informed Consent Statement:** Not applicable.

**Data Availability Statement:** Not applicable.

**Acknowledgments:** The authors thank David Kästner for his technical support.

**Conflicts of Interest:** The authors declare no conflict of interest.

## References

1. Taghinejad, M.; Cai, W. All-Optical Control of Light in Micro- and Nanophotonics. *ACS Photonics* **2019**, *6*, 1082–1093. [[CrossRef](#)]
2. Kurumida, J.; Yoo, S.J.B. Nonlinear Optical Signal Processing in Optical Packet Switching Systems. *IEEE J. Sel. Top. Quantum Electron.* **2012**, *18*, 978–987. [[CrossRef](#)]
3. Dvornikov, A.S.; Walker, E.P.; Rentzepis, P.M. Two-Photon Three-Dimensional Optical Storage Memory. *J. Phys. Chem. A* **2009**, *113*, 13633–13644. [[CrossRef](#)]
4. Walter, F.; Li, G.; Meier, C.; Zhang, S.; Zentgraf, T. Ultrathin Nonlinear Metasurface for Optical Image Encoding. *Nano Lett.* **2017**, *17*, 3171–3175. [[CrossRef](#)] [[PubMed](#)]
5. Palomba, S.; Novotny, L. Near-Field Imaging with a Localized Nonlinear Light Source. *Nano Lett.* **2009**, *9*, 3801–3804. [[CrossRef](#)] [[PubMed](#)]
6. Gadhwal, R.; Devi, A. A review on the development of optical limiters from homogeneous to reflective 1-D photonic crystal structures. *Opt. Laser Technol.* **2021**, *141*, 107144. [[CrossRef](#)]
7. Zhang, X.; Zhang, D.; Tan, D.; Xian, Y.; Liu, X.; Qiu, J. Highly Defective Nanocrystals as Ultrafast Optical Switches: Nonequilibrium Synthesis and Efficient Nonlinear Optical Response. *Chem. Mater.* **2020**, *32*, 10025–10034. [[CrossRef](#)]
8. Liu, G.; You, S.; Ma, M.; Huang, H.; Ren, N. Removal of Nitrate by Photocatalytic Denitrification Using Nonlinear Optical Material. *Environ. Sci. Technol.* **2016**, *50*, 11218–11225. [[CrossRef](#)]
9. Kulyk, B.; Essaidi, Z.; Kapustianyk, V.; Turko, B.; Rudyk, V.; Partyka, M.; Addou, M.; Sahraoui, B. Second and third order nonlinear optical properties of nanostructured ZnO thin films deposited on a-BBO and LiNbO<sub>3</sub>. *Opt. Commun.* **2008**, *281*, 6107–6111. [[CrossRef](#)]
10. Zhang, Y.-x.; Wang, Y.-h. Nonlinear optical properties of metal nanoparticles: A review. *RSC Adv.* **2017**, *7*, 45129–45144. [[CrossRef](#)]
11. You, J.W.; Bongu, S.R.; Bao, Q.; Panoiu, N.C. Nonlinear optical properties and applications of 2D materials: Theoretical and experimental aspects. *Nanophotonics* **2019**, *8*, 63–97. [[CrossRef](#)]
12. Lehr, D.; Reinhold, J.; Thiele, I.; Hartung, H.; Dietrich, K.; Menzel, C.; Pertsch, T.; Kley, E.-B.; Tünnermann, A. Enhancing Second Harmonic Generation in Gold Nanoring Resonators Filled with Lithium Niobate. *Nano Lett.* **2015**, *15*, 1025–1030. [[CrossRef](#)]
13. Sánchez-Dena, O.; Mota-Santiago, P.; Tamayo-Rivera, L.; García-Ramírez, E.V.; Crespo-Sosa, A.; Oliver, A.; Reyes-Esqueda, J.-A. Size- and shape-dependent nonlinear optical response of Au nanoparticles embedded in sapphire. *Opt. Mater. Express* **2014**, *4*, 92. [[CrossRef](#)]
14. Sato, R.; Ohnuma, M.; Oyoshi, K.; Takeda, Y. Experimental investigation of nonlinear optical properties of Ag nanoparticles: Effects of size quantization. *Phys. Rev. B* **2014**, *90*, 125417. [[CrossRef](#)]



15. Che, F.; Grabtchak, S.; Whelan, W.M.; Ponomarenko, S.A.; Cada, M. Relative SHG measurements of metal thin films: Gold, silver, aluminum, cobalt, chromium, germanium, nickel, antimony, titanium, titanium nitride, tungsten, zinc, silicon and indium tin oxide. *Results Phys.* **2017**, *7*, 593–595. [[CrossRef](#)]
16. Alam, M.Z.; de Leon, I.; Boyd, R.W. Large Optical Nonlinearity of Indium Tin Oxide in its Epsilon-Near-Zero Region. *Science* **2016**, *352*, 795–797. [[CrossRef](#)] [[PubMed](#)]
17. Wickberg, A.; Kieninger, C.; Sürgers, C.; Schlabach, S.; Mu, X.; Koos, C.; Wegener, M. Second-Harmonic Generation from ZnO/Al<sub>2</sub>O<sub>3</sub> Nanolaminate Optical Metamaterials Grown by Atomic-Layer Deposition. *Adv. Opt. Mater.* **2016**, *4*, 1203–1208. [[CrossRef](#)]
18. Alloatti, L.; Kieninger, C.; Froelich, A.; Lauermann, M.; Frenzel, T.; Köhnle, K.; Freude, W.; Leuthold, J.; Wegener, M.; Koos, C. Second-order nonlinear optical metamaterials: ABC-type nanolaminates. *Appl. Phys. Lett.* **2015**, *107*, 121903. [[CrossRef](#)]
19. Probst, A.-C.; Stollenwerk, M.; Emmerich, F.; Büttner, A.; Zeising, S.; Stadtmüller, J.; Riethmüller, F.; Stehlíková, V.; Wen, M.; Proserpio, L.; et al. Influence of sputtering pressure on the nanostructure and the X-ray reflectivity of iridium coatings. *Surf. Coat. Technol.* **2018**, *343*, 101–107. [[CrossRef](#)]
20. Henriksen, P.L.; Ferreira, D.D.M.; Massahi, S.; Civitani, M.C.; Basso, S.; Vogel, J.; Armendariz, J.R.; Knudsen, E.B.; Irastorza, I.G.; Christensen, F.E. Iridium thin-film coatings for the BabyIAXO hybrid X-ray optic. *Appl. Opt.* **2021**, *60*, 6671–6681. [[CrossRef](#)] [[PubMed](#)]
21. Arblaster, J.W. Crystallographic Properties of Iridium. *Platin. Met. Rev.* **2010**, *54*, 93–102. [[CrossRef](#)]
22. Vila-Comamala, J.; Gorelick, S.; Färm, E.; Kewish, C.M.; Diaz, A.; Barrett, R.; Guzenko, V.A.; Ritala, M.; David, C. Ultra-High Resolution Zone-Doubled Diffractive X-ray Optics for the Multi-keV Regime. *Opt. Express* **2011**, *19*, 175–184. [[CrossRef](#)]
23. Weber, T.; Käsebier, T.; Szeghalmi, A.; Knez, M.; Kley, E.-B.; Tünnermann, A. Iridium Wire Grid Polarizer Fabricated using Atomic Layer Deposition. *Nanoscale Res. Lett.* **2011**, *6*, 558. [[CrossRef](#)]
24. Hemphill, R.; Hurwitz, M.; Pelizzo, M.G. Osmium Atomic-Oxygen Protection by an Iridium Overcoat for Increased Extreme-Ultraviolet Grating Efficiency. *Appl. Opt.* **2003**, *42*, 5149–5157. [[CrossRef](#)]
25. Schmitt, P.; Felde, N.; Döhring, T.; Stollenwerk, M.; Uschmann, I.; Hanemann, K.; Siegler, M.; Klemm, G.; Gratzke, N.; Tünnermann, A.; et al. Optical, Structural, and Functional Properties of Highly Reflective and Stable Iridium Mirror Coatings for Infrared Applications. *Opt. Mater. Express* **2021**, *12*, 545–559. [[CrossRef](#)]
26. Colombo, A.; Dragonetti, C.; Guerchais, V.; Hierlinger, C.; Zysman-Colman, E.; Roberto, D. A trip in the nonlinear optical properties of iridium complexes. *Coord. Chem. Rev.* **2020**, *414*, 213293. [[CrossRef](#)]
27. Yan, L.; Woollam, J.A. Optical constants and roughness study of dc magnetron sputtered iridium films. *J. Appl. Phys.* **2002**, *92*, 4386–4392. [[CrossRef](#)]
28. Kohli, S.; Niles, D.; Rithner, C.D.; Dorhout, P.K. Structural and optical properties of Iridium films annealed in air. *Adv. X-ray Anal.* **2002**, *45*, 352–358.
29. Ghazaryan, L.; Pfeiffer, K.; Schmitt, P.; Beladiya, V.; Kund, S.; Szeghalmi, A. Atomic Layer Deposition. In *Digital Encyclopedia of Applied Physics*; Wiley-VCH: Weinheim, Germany, 2020; pp. 1–44. ISBN 9783527600434.
30. Paul, P.; Hafiz, M.G.; Schmitt, P.; Patzig, C.; Otto, F.; Fritz, T.; Tünnermann, A.; Szeghalmi, A. Optical Bandgap Control in Al<sub>2</sub>O<sub>3</sub>/TiO<sub>2</sub> Heterostructures by Plasma Enhanced Atomic Layer Deposition: Toward Quantizing Structures and Tailored Binary Oxides. *Spectrochim. Acta A Mol. Biomol. Spectrosc.* **2021**, *252*, 119508. [[CrossRef](#)] [[PubMed](#)]
31. Kuppadaakkath, A.; Najafidehaghani, E.; Gan, Z.; Tuniz, A.; Ngo, G.Q.; Knopf, H.; Löchner, F.J.F.; Abtahi, F.; Bucher, T.; Shradha, S.; et al. Direct growth of monolayer MoS<sub>2</sub> on nanostructured silicon waveguides. *Nanophotonics* **2022**, *11*, 4397–4408. [[CrossRef](#)]
32. Schmitt, P.; Beladiya, V.; Felde, N.; Paul, P.; Otto, F.; Fritz, T.; Tünnermann, A.; Szeghalmi, A.V. Influence of Substrate Materials on Nucleation and Properties of Iridium Thin Films Grown by ALD. *Coatings* **2021**, *11*, 173. [[CrossRef](#)]
33. Daryakar, N.; David, C. Thin Films of Nonlinear Metallic Amorphous Composites. *Nanomaterials* **2022**, *12*, 3359. [[CrossRef](#)] [[PubMed](#)]
34. Genevée, P.; Ahiavi, E.; Janunts, N.; Pertsch, T.; Oliva, M.; Kley, E.-B.; Szeghalmi, A. Blistering during the atomic layer deposition of iridium. *J. Vac. Sci. Technol. A* **2016**, *34*, 01A113. [[CrossRef](#)]
35. ImageJ. Available online: <https://imagej.nih.gov/ij/> (accessed on 10 September 2020).
36. Schröder, S.; Herffurth, T.; Blaschke, H.; Duparré, A. Angle-resolved scattering: An effective method for characterizing thin-film coatings. *Appl. Opt.* **2011**, *50*, C164–C171. [[CrossRef](#)]
37. Markel, V.A. Introduction to the Maxwell Garnett approximation: Tutorial. *JOSA A* **2016**, *33*, 1244–1256. [[CrossRef](#)] [[PubMed](#)]
38. Battie, Y.; Resano-Garcia, A.; Chaoui, N.; Zhang, Y.; En Naciri, A. Extended Maxwell-Garnett-Mie formulation applied to size dispersion of metallic nanoparticles embedded in host liquid matrix. *J. Chem. Phys.* **2014**, *140*, 44705. [[CrossRef](#)]
39. Sipe, J.E.; Boyd, R.W. Nonlinear susceptibility of composite optical materials in the Maxwell Garnett model. *Phys. Rev. A* **1992**, *46*, 1614–1629. [[CrossRef](#)] [[PubMed](#)]
40. Peiponen, K.-E.; Mäkinen, M.O.A.; Saarinen, J.J.; Asakura, T. Dispersion Theory of Liquids Containing Optically Linear and Nonlinear Maxwell Garnett Nanoparticles. *Opt. Rev.* **2001**, *8*, 9–17. [[CrossRef](#)]
41. Saarinen, J.J.; Vartiainen, E.M.; Peiponen, K.-E. On Tailoring of Nonlinear Spectral Properties of Nanocomposites Having Maxwell Garnett or Bruggeman Structure. *Opt. Rev.* **2003**, *10*, 111–115. [[CrossRef](#)]
42. Boyd, R.W.; Gehr, R.J.; Fischer, G.L.; Sipe, J.E. Nonlinear optical properties of nanocomposite materials. *Pure Appl. Opt. J. Eur. Opt. Soc. A* **1996**, *5*, 505–512. [[CrossRef](#)]



43. Boyd, R.W. *Nonlinear Optics*, 2nd ed.; Elsevier: Amsterdam, The Netherlands, 2003; ISBN 9780080479750.
44. Del Coso, R.; Solis, J. Relation between nonlinear refractive index and third-order susceptibility in absorbing media. *J. Opt. Soc. Am. B* **2004**, *21*, 640. [[CrossRef](#)]
45. Maniyara, R.A.; Rodrigo, D.; Yu, R.; Canet-Ferrer, J.; Ghosh, D.S.; Yongsunthon, R.; Baker, D.E.; Rezikyan, A.; García de Abajo, F.J.; Pruneri, V. Tunable Plasmons in Ultrathin Metal Films. *Nat. Photon.* **2019**, *13*, 328–333. [[CrossRef](#)]
46. Formica, N.; Ghosh, D.S.; Carrilero, A.; Chen, T.L.; Simpson, R.E.; Pruneri, V. Ultrastable and Atomically Smooth Ultrathin Silver Films Grown on a Copper Seed Layer. *ACS Appl. Mater. Interfaces* **2013**, *5*, 3048–3053. [[CrossRef](#)] [[PubMed](#)]
47. Zheng, X.; Zhang, Y.; Chen, R.; Cheng, X.; Xu, Z.; Jiang, T. Z-scan measurement of the nonlinear refractive index of monolayer WS(2). *Opt. Express* **2015**, *23*, 15616–15623. [[CrossRef](#)]
48. Milam, D. Review and assessment of measured values of the nonlinear refractive-index coefficient of fused silica. *Appl. Opt.* **1998**, *37*, 546–550. [[CrossRef](#)]
49. Schaffer, C.B.; Brodeur, A.; Mazur, E. Laser-induced breakdown and damage in bulk transparent materials induced by tightly focused femtosecond laser pulses. *Meas. Sci. Technol.* **2001**, *12*, 1784–1794. [[CrossRef](#)]
50. Guillet, Y.; Rashidi-Huyeh, M.; Palpant, B. Influence of laser pulse characteristics on the hot electron contribution to the third-order nonlinear optical response of gold nanoparticles. *Phys. Rev. B* **2009**, *79*, 45410. [[CrossRef](#)]
51. Moradi, A. Maxwell-Garnett effective medium theory: Quantum nonlocal effects. *Phys. Plasmas* **2015**, *22*, 42105. [[CrossRef](#)]
52. Boyd, R.W.; Shi, Z.; de Leon, I. The third-order nonlinear optical susceptibility of gold. *Opt. Commun.* **2014**, *326*, 74–79. [[CrossRef](#)]
53. Castro, H.P.S.; Wender, H.; Alencar, M.A.R.C.; Teixeira, S.R.; Dupont, J.; Hickmann, J.M. Third-order nonlinear optical response of colloidal gold nanoparticles prepared by sputtering deposition. *J. Appl. Phys.* **2013**, *114*, 183104. [[CrossRef](#)]
54. Hache, F.; Ricard, D.; Flytzanis, C.; Kreibig, U. The optical kerr effect in small metal particles and metal colloids: The case of gold. *Appl. Phys. A* **1988**, *47*, 347–357. [[CrossRef](#)]
55. Stepanov, A.L. Nonlinear Optical Properties of Metal Nanoparticles in Silicate Glass. In *Glass Nanocomposites: Synthesis, Properties and Applications*; Karmakar, B., Rademann, K., Stepanov, A.L., Eds.; William Andrew: Norwich, UK, 2016; pp. 165–179. ISBN 9780323393096.
56. Shen, H.; Cheng, B.; Lu, G.; Ning, T.; Guan, D.; Zhou, Y.; Chen, Z. Enhancement of optical nonlinearity in periodic gold nanoparticle arrays. *Nanotechnology* **2006**, *17*, 4274–4277. [[CrossRef](#)]
57. Bai, S.; Li, Q.; Zhang, H.; Chen, X.; Luo, S.; Gong, H.; Yang, Y.; Zhao, D.; Qiu, M. Large third-order nonlinear refractive index coefficient based on gold nanoparticle aggregate films. *Appl. Phys. Lett.* **2015**, *107*, 141111. [[CrossRef](#)]
58. Stenzel, O.; Wilbrandt, S.; Mühlig, C.; Schröder, S. Linear and Nonlinear Absorption of Titanium Dioxide Films Produced by Plasma Ion-Assisted Electron Beam Evaporation: Modeling and Experiments. *Coatings* **2020**, *10*, 59. [[CrossRef](#)]
59. Smith, D.D.; Yoon, Y.; Boyd, R.W.; Campbell, J.K.; Baker, L.A.; Crooks, R.M.; George, M. z-scan measurement of the nonlinear absorption of a thin gold film. *J. Appl. Phys.* **1999**, *86*, 6200–6205. [[CrossRef](#)]
60. Jia, L.; Cui, D.; Wu, J.; Feng, H.; Yang, Y.; Yang, T.; Qu, Y.; Du, Y.; Hao, W.; Jia, B.; et al. Highly nonlinear BiOBr nanoflakes for hybrid integrated photonics. *APL Photonics* **2019**, *4*, 90802. [[CrossRef](#)]

**Disclaimer/Publisher's Note:** The statements, opinions and data contained in all publications are solely those of the individual author(s) and contributor(s) and not of MDPI and/or the editor(s). MDPI and/or the editor(s) disclaim responsibility for any injury to people or property resulting from any ideas, methods, instructions or products referred to in the content.